System Identification with Biophysical Constraints: A Circuit Model of the Inner Retina

Cornelius Schröder[*]
University of Tübingen
cornelius.schroeder@uni-tuebingen.de

David Klindt[*]
University of Tübingen
david.klindt@bethgelab.org

Sarah Strauß
University of Tübingen
sarah.strauss@uni-tuebingen.de

Katrin Franke
University of Tübingen
katrin.franke@cin.uni-tuebingen.de

Matthias Bethge
University of Tübingen
matthias@bethgelab.org

Thomas Euler
University of Tübingen
thomas.euler@cin.uni-tuebingen.de

Philipp Berens
University of Tübingen
philipp.berens@uni-tuebingen.de

Abstract

Visual processing in the retina has been studied in great detail at all levels such that a comprehensive picture of the retina's cell types and the many neural circuits they form is emerging. However, the currently best performing models of retinal function are black-box CNN models which are agnostic to such biological knowledge. In particular, these models typically neglect the role of the many inhibitory circuits involving amacrine cells and the biophysical mechanisms underlying synaptic release. Here, we present a computational model of temporal processing in the inner retina, including inhibitory feedback circuits and realistic synaptic release mechanisms. Fit to the responses of bipolar cells, the model generalized well to new stimuli including natural movie sequences, performing on par with or better than a benchmark black-box model. In pharmacology experiments, the model replicated *in silico* the effect of blocking specific amacrine cell populations with high fidelity, indicating that it had learned key circuit functions. Also, more in depth comparisons showed that connectivity patterns learned by the model were well matched to connectivity patterns extracted from connectomics data. Thus, our model provides a biologically interpretable data-driven account of temporal processing in the inner retina, filling the gap between purely black-box and detailed biophysical modeling.

1 Introduction

In the retina, light is transduced by the photoreceptors (PRs) and processed in two layers of neuropil before the signal is sent to the brain (Fig. 1). In the outer plexiform layer, the output of PRs is shaped by feedback of horizontal cells before it is passed to the bipolar cells (BCs). In mice, 14 types of BC then relay the signal to the second synaptic layer, the inner plexiform layer (IPL). Here, the signal is

---

[*]Equal contribution.
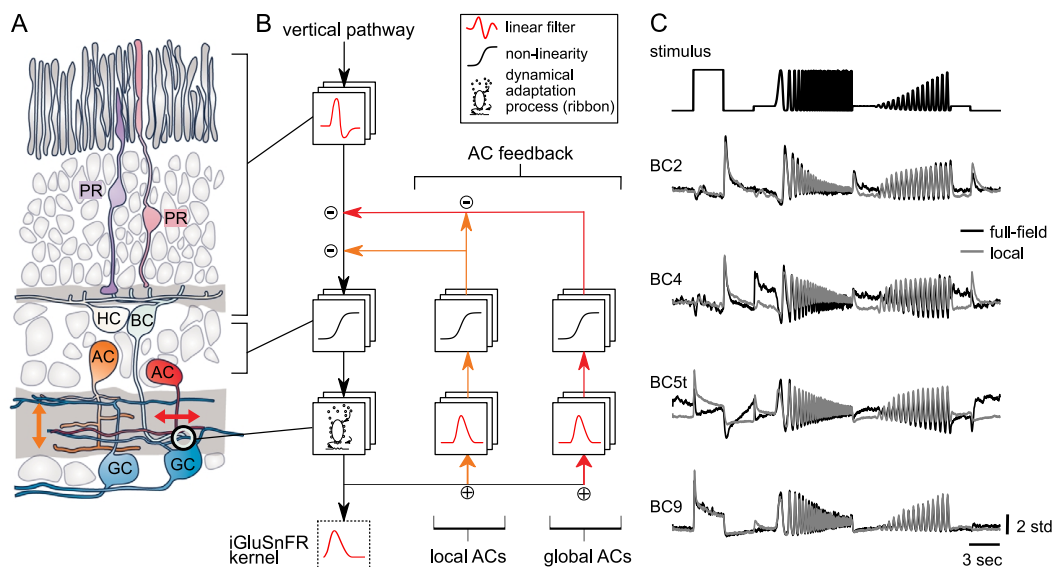
Figure 1: **Retinal circuit schematics. A.** The signalling pathways in the retina: photoreceptors (PRs) transmit the light signal to bipolar cells (BCs) before it is passed on to ganglion cells (GCs), which project the signal to the brain. In between, the signal is shaped by two classes of mostly inhibitory interneurons: horizontal cells (HCs) and amacrine cells (ACs). Figure adapted from [13]. **B.** Translation of the retinal circuit to a computational network model. We modeled two main groups of ACs: more globally and more locally acting feedback neurons. **C.** Light stimulus-evoked responses of four different types of BCs (two Off and two On cells); overlaid are traces for spatially extended (full-field) and localized (local) chirp stimuli. For details, see [5].

shaped by a complex network of more than 45 different types of mostly inhibitory amacrine cells (ACs) [1, 2, 3] and passed on to the retinal ganglion cells (RGCs), which in turn transmit the signals to visual areas in the brain. Already at the level of BCs, different parallel pathways emerge, which are tuned for specific features of the stimulus. While the different BC types have been well studied at the morphological, genetic and functional level [4, 5, 6], a comprehensive understanding of how the diverse AC types shape BC output is still missing and so far, only highly specialized AC circuits have been studied extensively [7, 2].

At the same time, the currently best-performing systems identification models for retinal neurons only account for feedforward drive and typically neglect ACs, even when mimicking the non-linear subunit structure of retinal processing [8, 9, 10, 11]. Therefore, our knowledge about the computational role of ACs is largely limited to basic principles: for example, GABA-releasing wide-field ACs mostly provide lateral feedback, while glycinergic small-field ACs predominantly mediate vertical feedback across different strata of the IPL and modulate wide-field AC input to BCs [2]. In addition, system identification models typically neglect well-understood biophysical mechanisms involved in temporal adaptation and therefore lack a clear link to the underlying biology. For example, the specialized ribbon synapse, a feature of PRs and BCs, is known to dramatically shape the temporal structure of the transmitted signal [12].

Here, we build on recent work modeling stimulus-response relationships of individual neurons extending simple linear-nonlinear models to a full-scale network model of the IPL while keeping a much higher degree of biophysical realism. Our contributions are:

1. We show how to train a network model of the IPL including ACs and a high degree of biophysical realism end-to-end to reproduce the temporal responses of all 14 mouse BC types on artificial stimuli (Figure 1 and 2).

2. We show that the predictive performance of this model is as good as that of deep recurrent models on artificial as well as on natural stimuli (Figure 3).

3. We perform *in silico* pharmacological modulations and show that blocking different groups of ACs has similar effects to what is observed in experiments (Figure 4).

2

4. We compare the connectivity between the different types of BCs and ACs in our model to connectomics data [14] and find that our model has learned the general rules of IPL connectivity from functional data (Figure 5).

5. Finally, we use the biological realistic components of the model to make predictions on biophysical properties of the ribbon synapses for individual BC types (Figure 6).

Thus, our model provides a biologically interpretable data-driven account of temporal processing in the inner retina, filling the gap between purely black-box modeling and detailed biophysical modeling.

2 Previous Work

Current models of neural processing in the retina broadly fall into two categories:

1. *Neural system identification* approaches [15] are designed to maximize the performance when predicting the activity of a retinal neuron or a population of neurons from the visual stimulus. Such models include statistical linear-nonlinear-Poisson models (LNP) and their generalizations incorporating feedback terms and non-linear subunits [8, 9] as well as models based on deep neural networks [11, 16, 17]. These approaches are able to predict the activity of retinal neurons with remarkable accuracy and subunits in the respective models can resemble presynaptic neurons [10, 18, 19, 20]. However, the models are often difficult to interpret in terms of actual biological mechanisms. In addition, they typically fail to model adaptive processes determining the temporal response kinetics in many retinal neurons.

2. *Mechanistic models* for retinal neurons are typically biophysically realistic models based on Hodgkin-Huxley equations. For example, such models have been used to model the activity of BCs and RGCs, and can do very well in accounting for adaptive processes, as they incorporate the underlying biophysical mechanisms [21, 22]. Such models are based on large amounts of biological detail and knowledge, thus enabling a mechanistic investigation into a specific computation, but are time-consuming to simulate and notoriously hard to fit to data.

To strike a middle ground between these two extremes, systems identification models have been combined with an additional kinetic block that allows them to account for rapid release adaptation at synaptic sites as well as other adaptive processes [23, 24]. Additionally, a single inhibitory pathway has been incorporated in such models to account for the aggregate feedback from all ACs [25]. Here, we advance such hybrid models and combine an interpretable linear-nonlinear-release (LNR) model with a kinetic block [24] with the rich feedback structure of the whole AC network. Using this network to model temporal processing in the IPL, we obtain accurate predictions of BC activity across a wide range of stimuli while maintaining a high degree of biological interpretability. In contrast to the often involved inference necessary for biophysically realistic models [22], our model is completely differentiable and can be efficiently learned end-to-end with modern deep learning frameworks.

3 Model

3.1 The Bipolar Cell Network model

Our BC network (BCN) model consists of two main parts: i) a vertical model of the 14 parallel BC channels, and ii) a model of the AC feedback (Fig. 1B). The feedback consists of a *local* and *global* pathway, activated by stimulation of center and surround component of BC receptive fields, respectively. As data, we used light-evoked responses of BCs recorded with the genetically encoded glutamate sensor iGluSnFr [5] (c.f. Appendix B). Therefore, we convolved our model output with the iGluSnFR kernel as a final step, which allows for a direct comparison to the functional recordings of BCs. In total, the model has 1,932 free parameters.

3.1.1 Model of the vertical pathway

The vertical pathway consists of a linear biphasic kernel, a sigmoidal non-linearity and a model of the release machinery at a ribbon synapse. The linear stage accounts for the approximately linear
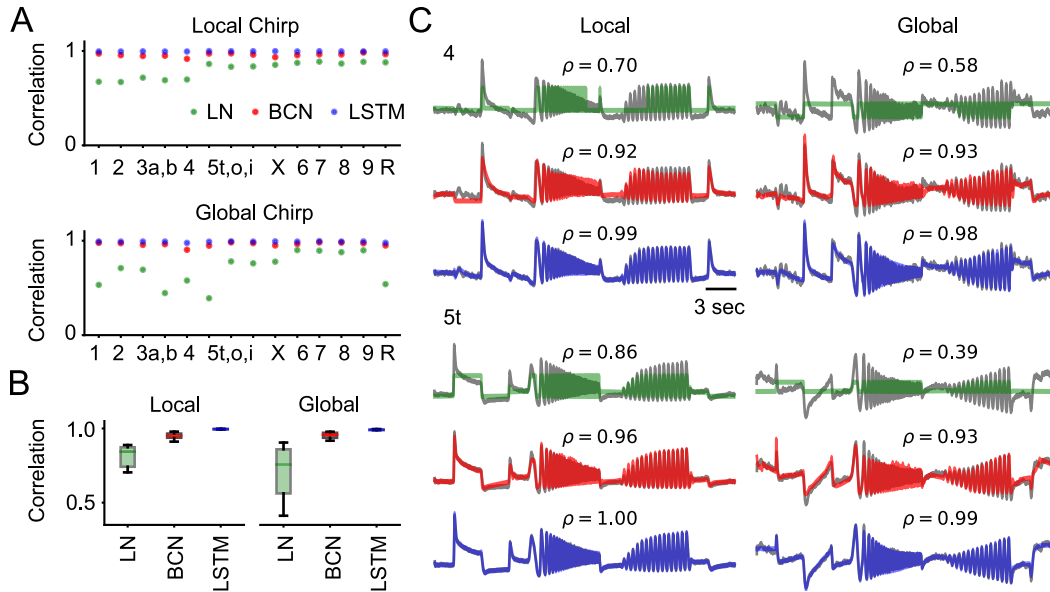
Figure 2: **Training Performance. A.** Linear correlation of the output of the three models for all 14 BC types on the local (top) and the global (bottom) chirp stimulus. **B.** Summary of the correlation across all types of BCs for the three models and two stimulus conditions. **C.** Model predictions for the Off (type 4) and On (type 5t) BC from Fig. 1C. Cluster mean traces are shown in grey and ρ gives Pearson correlation coefficients.

processing of light l in PRs and dendrites of BC i [26]:

$$\text{BC}_i^{\text{in}}(t) = \int_{\tau=0}^{T} l(t-\tau) \cdot \kappa_i^{\text{PR}}(\tau)d\tau.$$

The signal is then modulated by the local and global AC feedback ($\text{fb}_i(t)$, see Section 3.1.2) before it is passed through a sigmoidal non-linearity to be converted into vesicle release probability p_i (see Appendix A for details):

$$p_i(t) = \sigma_i \left(\text{BC}_i^{\text{in}}(t) - \text{fb}_{\text{local},i}(t) - \text{fb}_{\text{global},i}(t) \right).$$

We mimic sensitivity adaptation in the retina by allowing the offset of the non-linearity to change by shifting its operating point [25]. This allows different computations in the vertical pathway for local and full-field stimuli. We used a deterministic version of the release model described in [24] to model the BC's synapse. In this model, vesicles move between three different pools in a probabilistic fashion: At each time step, vesicles are first released from the ready releasable pool (RRP), then new vesicles are moved from the intermediate pool (IP) to the RRP, and finally the IP is refilled from the cytoplasm. To make the model deterministic, we replaced all random variables by their expected value given the present state of the different pools. This results in three simplified equations for vesicle movement:
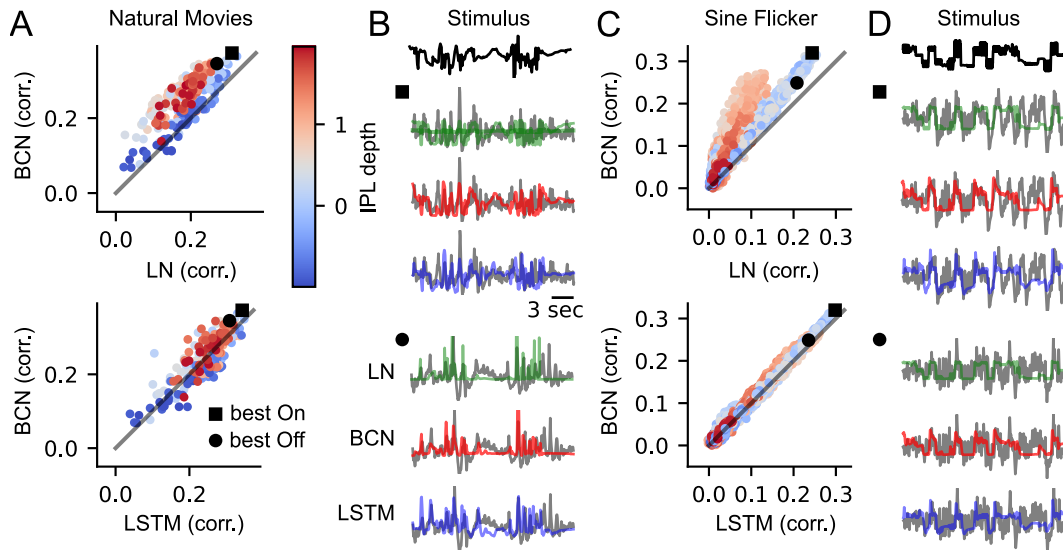
$$\text{release} = p(t) \cdot \text{RRP}, \qquad \text{RRP}_{\text{refill}} = k_1 \cdot \text{IP}, \qquad \text{IP}_{\text{refill}} = k_2,$$

where k_1 and k_2 are constant over time. Additionally, maximal pool sizes were learned for the IP and RRP. For better training performance, the occupancies of the pools were sent through a sigmoidal non-linearity in in each time step and thus smoothly clamped at the maximal values.

3.1.2 Feedback model

The feedback structure is implemented by a network of ACs (Fig. 1B). Each AC is modeled by a LN model, which receives input from all BC types with learned weights $W^{\text{BC AC}}$. The LN part consists of a double-exponential kernel κ^{AC} (see Appendix A for details) and a sigmoidal non-linearity σ afterwards:

$$\text{AC}_i^{\text{out}}(t) = \sigma_i \left(\int_{\tau=0}^{T} \left(\sum_{j=1}^{14} w_{ij}^{\text{BC AC}} \cdot \text{BC}_j^{\text{out}}(t-\tau) \right) \cdot \kappa_i^{\text{AC}}(\tau)d\tau \right).$$

4

Figure 3: **Generalization Performance.** **A.** Each point corresponds to the Pearson correlation between recorded response and model response of a single BC terminal for the LN model (x axis) and BCN model (y axis). Color indicates IPL depth (center at 0.5), straight line the identity. IPL depth is a good proxy for On/Off separation, Off BCs are in higher depth (red), On cells deeper (blue). **B.** Sample predictions for the best On and Off BC terminal (highest correlation across all models) for the three models (recorded traces in grey). **C., D.** Same as A, B but for a sine flicker stimulus of varying size. Note that the IPL depth had to be estimated differently for these recordings, which might cause a difference in scaling compared to A. The dense regions of the stimulus have high frequency sinusoidal oscillations.

We modeled both the local and global AC pathways, consisting of mostly glycinergic and mostly GABAergic ACs, respectively. While both groups provide direct feedback to most BCs, local ACs also act as a gate keeper for global ACs by modulating their output to BCs in an inhibitory manner (cf. Figure 1B, [13]). The two AC groups further differ in their spatial tuning. Local ACs integrate over small spatial regions (up to $300\mu m$ [2, 13]), whereas global ACs are better activated by larger stimuli, complementing their smaller counterparts. Consequently in the model, global feedback is only activated during full-field stimuli, whereas local feedback is present for all stimuli. We can thus describe the feedback for each BC i in the following way:

$$\text{fb}_{\text{local},i}(t) = \sum_j w_{ij}^{\text{AC}_{\text{local}}\text{BC}} \cdot \text{AC}_{\text{local},j}^{\text{out}}(t) \qquad \text{and}$$

$$\text{fb}_{\text{global},i}(t) = \mathbb{1}_{\text{global}} \cdot \left(\sum_j w_{ij}^{\text{AC}_{\text{global}}\text{BC}} \cdot \text{AC}_{\text{global},j}^{\text{out}}(t) - \sum_j w_{ij}^{\text{AC}_{\text{local}}\text{AC}_{\text{global}}} \cdot \text{AC}_{\text{local},j}^{\text{out}}(t) \right).$$

To be able to compare the learned connectivity structure, which is represented by the different weight matrices W, with the connectivity structure found in electronmicroscopy data, we took the number of ACs from [14] (45 ACs in total) and matched the ratio of local to global ACs to the ones identified in [3] (10:35) (see Appendix F for details).

3.2 Benchmark models

LN model   As a lower bound for performance, we used a linear-nonlinear model (LN). It consists only of the two first stages of the LNR model. It has the same parameterization but does not incorporate any feedback. Its parameters were optimized using the same training schedule (c.f. Appendix C) as for the BCN model.

LSTM   As an upper bound for performance, we used a standard long-short-term-memory (LSTM) model (implemented in pytorch with `torch.LSTMModel`) with 18 hidden dimensions, and a linear readout layer with 28 output dimensions for the 14 local and 14 global traces, respectively. The
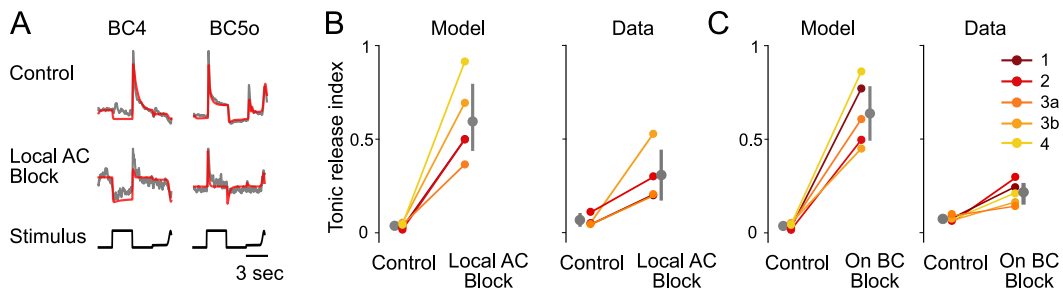
Figure 4: *In silico* **pharmacological experiments. A.** The model reproduces type-specific modulations of BC responses induced by drug application, all showing local responses (model in red, data in grey). **B.** Tonic release index for Off BCs under control condition and blocking of glycinergic (local) ACs (errorbars indicating bootstrapped 95% confidence intervals, Model: p=0.004 for a paired t-test). **C.** Tonic release index for Off BCs under control condition and blocking of the On BC pathway (Model: p=0.002 for a paired t-test). All figures of experimental data adapted from [5].

number of hidden dimensions was chosen such that the number of parameters (2,044) approximately matched the number of parameters of the BCN. The LSTM was trained on full length chirp traces. See Appendix C for details.

3.3 Training

The models were trained on the mean traces of the 14 BC types in response to local/global chirp stimulus (Fig. 1C). The data was recorded in the IPL using two-photon imaging of BC output with the genetically encoded fluorescent glutamate sensor iGluSnFr and clustered into functional types using an anatomy-guided clustering approach [5] (Appendix B). The training objective was to maximize the correlation between model predictions and recorded responses across all cell types and stimuli (local and global chirp). Letting $y_{i,s}, \hat{y}_{i,s}$ denote the (mean-centered) recorded and predicted response of type i to stimulus s, our loss function was

$$\mathcal{L}_{correlation} = -\sum_{i=1}^{14} \sum_{s \in \{local, global\}} \frac{y_{i,s}^T \hat{y}_{i,s}}{||y_{i,s}||_2 ||\hat{y}_{i,s}||_2} \,.$$

We minimized this loss function to train the LN and LSTM model.[2] For the BCN model, we encouraged sparse connections between different types of neurons as observed in real EM data [14], by additionally adding a sparse penalty, minimizing the 1-norm of all connectivity matrices W^j: $\mathcal{L}_{sparsity} = \sum_j ||W^j||_1$. Finally, we weighted the two terms and optimized $\mathcal{L}_{total} = \mathcal{L}_{correlation} + \beta\mathcal{L}_{sparsity}$. All models were written in PyTorch [27] and optimized using the Adam optimizer [28] (see Appendix C for details about hyper-parameter search and learning schedule).

4 Results

4.1 Model Performance

We found that the BCN model learned to predict BC chirp responses for both local and global chirps nearly perfectly when evaluated on the training data, with performance reaching almost that of the LSTM model (Fig. 2A, B; Table 1). In contrast, the LN model performed noticeably worse, failing to capture salient response features such as a slowly decaying response during the first onset of light (Fig. 2C). The BCN model was able to model this adaptative process accurately. While the LSTM model likewise captured this process and even achieved slightly higher correlation values, it showed signs of over-fitting as it predicted little noise ripples in the data (Fig. 2C, 4, left) .

---

[2]As two-photon imaging data is on an arbitrary scale, we did not learn the final linear transformation that minimizes the squared error of our model predictions $\sum_t (y_t - a_t\hat{y}_t)^2$. This linear transformation can simply be computed after fitting by setting $a_t = \frac{y_t}{\hat{y}_t}$.
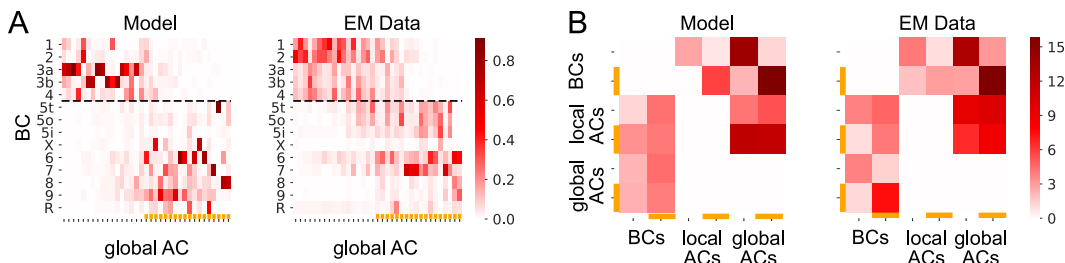
Figure 5: **Connectivity analysis. A.** Example weights of the best model and the EM data from [14] for BC to AC_{global} connectivity $W^{BC\,AC_{global}}$. See Appendix F for the full weight matrices. Orange lines indicating classification as On-cell. **B.** Connectivity matrices reduced to On/Off entries.

To probe the generalization performance of the model to unseen stimuli, we used additional recordings of BC terminals in response to natural movies and to sinusoidal flickering stimuli of constant and varying spatial size. To obtain a time series approximating the contrast statistics across the spatial receptive field of a single BC for the spatially inhomogeneous stimuli, we filtered these stimuli with a spatial difference of Gaussian kernel (see Appendix B) .

We found that the BCN performed better than the LN model and as good or better than the LSTM on the hold out data (Fig. 3; Table 1). In particular, we found a more pronounced performance gain for Off compared to On BCs. Note that in general, the correlation levels are lower than for the chirp data, as for both stimuli we had only few (natural movies) or even just one (sine stimulus) repetition and data was not averaged across recorded terminals. Additional data sets with variations of the sine stimuli are shown in Appendix D.

4.2 *In silico* Pharmacological Manipulations

We tested three different pharmacological manipulations *in silico* and compared their effects to previously obtained experimental results [5]. See Appendix E for details of the implementation. Blocking of local feedback led to more transient responses in On BCs and an increased modulation of release below baseline for Off BCs, in line with experimental findings (Fig. 4A, B). This is thought to result from an increase in tonic glutamate release caused by blocking cross-over inhibition from the On pathway mediated by small-field, glycinergic ACs. To confirm this idea, we additionally *in silico* blocked On BCs, that provide the excitatory drive for cross-over inhibition, and observed similar effects consistent with experimental data (Fig. 4C). This suggests that our model learned the circuit motif of cross-over inhibition. In addition, blocking local feedback decreased the correlation of local and global chirp responses of model BCs significantly ($p = 0.036$) due to dis-inhibition of global feedback (Appendix E). While the decrease in correlation was less pronounced in the model compared to experimental BC responses, this suggests that the model learned the gating of global by local feedback. Finally, blocking global feedback instead resulted in an increase in correlation between local and global chirp responses compared to the control condition, matching experimental data (Appendix E).

Table 1: **Training and generalization performance.** All numbers indicate mean Pearson's correlation, standard deviations are written in brackets (minimum clipped to 0.01). Best model in each column indicated in bold.

| Model | Training | | Generalization | | | |
	Local Chirp	Global Chirp	Natural	Vary Sine	Small Sine	Large Sine
LN	0.80 (0.09)	0.70 (0.17)	0.18 (0.06)	0.06 (0.05)	0.02 (0.02)	0.02 (0.02)
LSTM	**1.00** (0.01)	**0.99** (0.01)	**0.24** (0.06)	0.09 (0.07)	**0.03** (0.03)	0.03 (0.03)
BCN	0.96 (0.02)	0.96 (0.02)	**0.24** (0.06)	**0.10** (0.08)	**0.03** (0.03)	**0.04** (0.03)

4.3 Connectivity Analysis

Next, we compared the connectivity weights in our model to the connectivity of the IPL. For this, we used an EM data set consisting of all contacts between neurons of the inner retina [14] (for processing of the data set, see Appendix F). These contacts only represent potential synaptic contacts, as the data set does not contain any synaptic markers.

In order to compare ACs between model weights and connectivity data, we ordered them according to the ratio of Off to On BC input (Fig. 5A). ACs which predominately received input from On BCs were classified as On ACs, and vice versa.The connectivity matrices revealed a block diagonal structure in both the model and the EM data (Fig. 5A; see Appendix Fig. 10 for full connectivity matrix), which was even more striking if all connections of cells with same response polarity (On/Off) were combined (Fig. 5B). This suggests that feedback across On and Off layer is an important processing feature in the IPL. Overall, the learned connectivity weights were slightly sparser than in the EM data (Fig. 9A). To assess whether the similarity between model and EM connectivity matrix was due to chance, we constructed a random connectivity model, in which we drew random samples for each entry from the EM data distribution and preprocessed the matrix in the same way as before. However, the correlation of the model connectivity and the EM data was significantly higher than the correlation with the random model (Fig. 9B,C, $p = 0.019$, $p = 0.002$ for the best model respectively). We also found that the fraction of On ACs among global ACs (Fig. 9D) and the ratio of On to Off AC input to the BCs (Fig. 9 E) matched the EM data well. In contrast, the fraction of On ACs among local ACs was more comparable to the random model, suggesting that this feature of IPL connectivity could not be learned from the current limited functional data.

4.4 Model-based Prediction of Biophysical Properties

Finally, we show how our interpretable BCN model can be used to make predictions about cellular properties on the biophysical level. Inspecting the model parameters for the synaptic release of BCs, we found that RRP capacity was correlated with the global transience index (Pearson, $\rho = 0.48$, $p < 10^{-10}$, 20 best models, Fig. 6A), a measure of the ratio of activity decay after a large activation (computed on the experimental data; for details, see [5]). Interestingly, the RRP capacity together with the transfer rate from IP to RRP divided the BC types into clearly distinguishable clusters (Fig. 6B), suggesting that measuring these parameters experimentally would be important for understanding the emergence of different temporal processing channels in the inner retina.
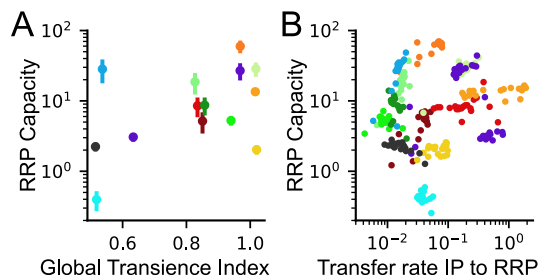

Figure 6: **Model-based Predictions. A.** Global transience index (as in [5]) and RRP capacity of the ribbon block. **B.** Model parameters of the ribbon block by BC type for the best 20 models. Red/yellow Off BCs, blue/green On BCs. See Appendix E for detailed color code.

5 Discussion

We trained a network model of temporal processing in the IPL including known structural constraints as well as biophysically inspired mechanisms to predict the functionally distinct responses of all 14 mouse BC types to different stimuli. It generalizes well and performs on par with a recurrent black-box model. Importantly, *in silico* pharmacology manipulations revealed that the model learned "cross-over inhibition" and "gating of global by local feedback" from the functional data, two of the central circuit motifs of the IPL. In addition, the connectivity structure of the model closely resembled that found in EM data. Furthermore, the model predicts that the 14 BC types can be clearly distinguished by the parameters of their synaptic release cascade, a prediction which remains to be tested. We emphasize that such predictions would not be easily possible from a pure systems identification approach.

Of course, our BCN model is but a first step in a comprehensive model of the IPL. On a technical level, it would be highly desirable to perform inference for BCN parameters using recent advances in Approximate Bayesian Computation [29, 30]. However, these approaches are typically limited to

models with dozens of parameters [22, 24]. When the technical challenges involved have been solved, this will allow for the identification of degenerate solutions and dependencies in the parameter space. Further, the BCN neglects most forms of more involved spatial processing or processing across light levels. In both cases, different sets of ACs are recruited across different stimulus conditions [2]. Therefore, including data from such conditions may be key in further understanding in how far the connectivity structure of the IPL follows computational demands.

Broader Impact

We present a model for temporal processing in the inner retina that combines system identification approaches with biophysically interpretable modules. The investigation of these modules allowed us to not only reproduce earlier experimental observations but also make predictions for the underlying biological system. First, this firmly grounds predictive models of neural activity in the biology of the underlying neural system, which is of high interest from a theoretical perspective. Second, the developed techniques for combining predictive and mechanistic models can likely be applied in other regions of the central nervous system, as the necessary data to provide the mechanistic constraints become available. Finally, our model may provide a first step towards establishing data driven *in silico* experiments for assessing the mechanisms of retinal degeneration and may inform future generations of targeted therapies aimed at curing the underlying diseases. At this time, we cannot envision any negative consequences to arise of this research.

Acknowledgments and Disclosure of Funding

References

[1] Richard H Masland. The fundamental plan of the retina. *Nature neuroscience*, 4(9):877–886, 2001.

[2] Jeffrey S Diamond. Inhibitory interneurons in the retina: types, circuitry, and function. *Annual review of vision science*, 3:1–24, 2017.

[3] Wenjun Yan, Mallory A Laboulaye, Nicholas M Tran, Irene E Whitney, Inbal Benhar, and Joshua R Sanes. Molecular identification of sixty-three amacrine cell types completes a mouse retinal cell atlas. *bioRxiv*, 2020.

[4] Christian Behrens, Timm Schubert, Silke Haverkamp, Thomas Euler, and Philipp Berens. Connectivity map of bipolar cells and photoreceptors in the mouse retina. *Elife*, 5:e20041, 2016.

[5] Katrin Franke, Philipp Berens, Timm Schubert, Matthias Bethge, Thomas Euler, and Tom Baden. Inhibition decorrelates visual feature representations in the inner retina. *Nature*, 542(7642):439–444, 2017.

[6] Karthik Shekhar, Sylvain W Lapan, Irene E Whitney, Nicholas M Tran, Evan Z Macosko, Monika Kowalczyk, Xian Adiconis, Joshua Z Levin, James Nemesh, Melissa Goldman, et al. Comprehensive classification of retinal bipolar neurons by single-cell transcriptomics. *Cell*, 166(5):1308–1323, 2016.

[7] Richard H Masland. The tasks of amacrine cells. *Visual neuroscience*, 29(1):3–9, 2012.

[8] Jonathan W Pillow, Jonathon Shlens, Liam Paninski, Alexander Sher, Alan M Litke, EJ Chichilnisky, and Eero P Simoncelli. Spatio-temporal correlations and visual signalling in a complete neuronal population. *Nature*, 454(7207):995–999, 2008.

[9] Qing Shi, Pranjal Gupta, Alexandra K Boukhvalova, Joshua H Singer, and Daniel A Butts. Functional characterization of retinal ganglion cells using tailored nonlinear modeling. *Scientific reports*, 9(1):1–12, 2019.

[10] Niru Maheswaranathan, David B Kastner, Stephen A Baccus, and Surya Ganguli. Inferring hidden structure in multilayered neural circuits. *PLoS computational biology*, 14(8):e1006291, 2018.

[11] Lane McIntosh, Niru Maheswaranathan, Aran Nayebi, Surya Ganguli, and Stephen Baccus. Deep learning models of the retinal response to natural scenes. In *Advances in neural information processing systems*, pages 1369–1377, 2016.

[12] Leon Lagnado and Frank Schmitz. Ribbon synapses and visual processing in the retina. *Annual review of vision science*, 1:235–262, 2015.

[13] Katrin Franke and Tom Baden. General features of inhibition in the inner retina. *The Journal of physiology*, 595(16):5507–5515, 2017.

[14] Moritz Helmstaedter, Kevin L Briggman, Srinivas C Turaga, Viren Jain, H Sebastian Seung, and Winfried Denk. Connectomic reconstruction of the inner plexiform layer in the mouse retina. *Nature*, 500(7461):168–174, 2013.

[15] Michael C-K Wu, Stephen V David, and Jack L Gallant. Complete functional characterization of sensory neurons by system identification. *Annu. Rev. Neurosci.*, 29:477–505, 2006.

[16] Eleanor Batty, Josh Merel, Nora Brackbill, Alexander Heitman, Alexander Sher, Alan Litke, EJ Chichilnisky, and Liam Paninski. Multilayer recurrent network models of primate retinal ganglion cell responses. 2016.

[17] David Klindt, Alexander S Ecker, Thomas Euler, and Matthias Bethge. Neural system identification for large populations separating "what" and "where". In *Advances in Neural Information Processing Systems*, pages 3506–3516, 2017.

[18] Esteban Real, Hiroki Asari, Tim Gollisch, and Markus Meister. Neural circuit inference from function to structure. *Current Biology*, 27(2):189–198, 2017.

[19] Jeremy Freeman, Greg D Field, Peter H Li, Martin Greschner, Deborah E Gunning, Keith Mathieson, Alexander Sher, Alan M Litke, Liam Paninski, Eero P Simoncelli, et al. Mapping nonlinear receptive field structure in primate retina at single cone resolution. *Elife*, 4:e05241, 2015.

[20] Nishal P Shah, Nora Brackbill, Colleen E Rhoades, Alexandra Kling, Georges Goetz, Alan Litke, Alexander Sher, Eero P Simoncelli, and EJ Chichilnisky. Inference of nonlinear spatial subunits by spike-triggered clustering in primate retina. *bioRxiv*, page 496422, 2019.

[21] JF Fohlmeister and RF Miller. Impulse encoding mechanisms of ganglion cells in the tiger salamander retina. *Journal of neurophysiology*, 78(4):1935–1947, 1997.

[22] Jonathan Oesterle, Christian Behrens, Cornelius Schröder, Thoralf Herrmann, Thomas Euler, Katrin Franke, Robert G Smith, Guenther Zeck, and Philipp Berens. Bayesian inference for biophysical neuron models enables stimulus optimization for retinal neuroprosthetics. *bioRxiv*, 2020.

[23] Yusuf Ozuysal and Stephen A Baccus. Linking the computational structure of variance adaptation to biophysical mechanisms. *Neuron*, 73(5):1002–1015, 2012.

[24] Cornelius Schröder, Ben James, Leon Lagnado, and Philipp Berens. Approximate bayesian inference for a mechanistic model of vesicle release at a ribbon synapse. In *Advances in Neural Information Processing Systems*, pages 7068–7078, 2019.

[25] David B Kastner, Yusuf Ozuysal, Georgia Panagiotakos, and Stephen A Baccus. Adaptation of inhibition mediates retinal sensitization. *Current Biology*, 29(16):2640–2651, 2019.

[26] Thomas Euler, Silke Haverkamp, Timm Schubert, and Tom Baden. Retinal bipolar cells: elementary building blocks of vision. *Nature Reviews Neuroscience*, 15(8):507–519, 2014.

[27] Adam Paszke, Sam Gross, Francisco Massa, Adam Lerer, James Bradbury, Gregory Chanan, Trevor Killeen, Zeming Lin, Natalia Gimelshein, Luca Antiga, et al. Pytorch: An imperative style, high-performance deep learning library. In *Advances in Neural Information Processing Systems*, pages 8024–8035, 2019.

[28] Diederik P Kingma and Jimmy Ba. Adam: A method for stochastic optimization. *arXiv preprint arXiv:1412.6980*, 2014.

[29] Pedro J Gonçalves, Jan-Matthis Lueckmann, Michael Deistler, Marcel Nonnenmacher, Kaan Öcal, Giacomo Bassetto, Chaitanya Chintaluri, William F Podlaski, Sara A Haddad, Tim P Vogels, et al. Training deep neural density estimators to identify mechanistic models of neural dynamics. *bioRxiv*, page 838383, 2019.

[30] George Papamakarios, David C Sterratt, and Iain Murray. Sequential neural likelihood: Fast likelihood-free inference with autoregressive flows. *arXiv preprint arXiv:1805.07226*, 2018.

[31] JL Schnapf, BJ Nunn, M Meister, and DA Baylor. Visual transduction in cones of the monkey macaca fascicularis. *The Journal of physiology*, 427(1):681–713, 1990.

[32] Tom Baden, Anton Nikolaev, Federico Esposti, Elena Dreosti, Benjamin Odermatt, and Leon Lagnado. A synaptic mechanism for temporal filtering of visual signals. *PLoS biology*, 12(10), 2014.

[33] Luke E Rogerson, Zhijian Zhao, Katrin Franke, Thomas Euler, and Philipp Berens. Bayesian hypothesis testing and experimental design for two-photon imaging data. *PLoS computational biology*, 15(8):e1007205, 2019.

[34] Zhijian Zhao, David A Klindt, André Maia Chagas, Klaudia P Szatko, Luke Rogerson, Dario A Protti, Christian Behrens, Deniz Dalkara, Timm Schubert, Matthias Bethge, et al. The temporal structure of the inner retina at a single glance. *Scientific reports*, 10(1):1–17, 2020.

[35] Margaret A. MacNeil, John K. Heussy, Ramon F. Dacheux, Elio Raviola, and Richard H. Masland. The shapes and numbers of amacrine cells: Matching of photofilled with golgi-stained cells in the rabbit retina and comparison with other mammalian species. *Journal of Comparative Neurology*, 413:305–326, 1999.

[36] Sammy C.S. Lee, Arndt Meyer, Timm Schubert, Larua Hüser, Karin Dedek, and Silke Haverkamp. Morphology and connectivity of the small bistratified a8 amacrine cell in the mouse retina. *Journal of Comparative Neurology*, 523:1529–1547, 2015.

[37] Heinz Wässle, Peter Koulen, Johann Helmut Brandstätter, Erica Fletcher, and Cord-Michael Becker. Glycine and gaba receptors in the mammalian retina. *Vision Research*, 38:1411–1430, 1998.

[38] Sonja Neumann and Silke Haverkamp. Characterization of small-field bistratified amacrine cells in macaque retina labeled by antibodies against synaptotagmin-2. *Journal of Comparative Neurology*, 521:709–724, 2013.

[39] Nicole Menger, David V. Pow, and Heinz Wässle. Glycinergic amacrine cells of the rat retina. *Journal of Comparative Neurology*, 401:34–46, 1998.

Appendix

A Model details

A.1 Vertical Pathway

The linear filter κ^{PR} in the vertical pathway was modeled as a biphasic filter [31, 32] which depends on a rise and decay constant (τ_r and τ_d) and additional phase parameters (ϕ and τ_{phase}). We used additionally one free parameter γ as in [24], which is stretching/compressing the kernel on the time axis and inferred from the data. This leads to the kernel

$$\kappa^{\text{PR}}(t, \gamma) = \frac{-\left(\frac{t}{\gamma \tau_r}\right)^3}{1 + \frac{t}{\gamma \tau_r}} \cdot \exp\left(-\left(\frac{t}{\gamma \tau_d}\right)^2\right) \cdot \cos\left(\frac{2\pi t}{\gamma \phi} + \tau_{\text{phase}}\right) \; ,$$

which was normalized to have norm one. The remaining parameters were held constant: $\tau_r = 0.05$, $\tau_d = 0.05$, $\tau_{\text{phase}} = 100$ and $\phi = -\pi/7$.

We used a sigmoidal non-linearity σ with two parameters for the offset and the slope (x_0 and k):

$$\sigma(x) = \frac{1}{1 + \exp(-k(x - x_0))} \; .$$

A.2 Amacrine Cell Feedback

The synaptic integration of ACs was modelled as a double exponential kernel κ_{AC} with two time parameters for rise and decay (τ_r and τ_d) per AC:

$$\kappa^{\text{AC}}(t) = \exp\left(\frac{-t}{\tau_d}\right) - \exp\left(\frac{-t \cdot (\tau_d + \tau_r)}{\tau_d \cdot \tau_r}\right) \; .$$

As non-linearity we took the same sigmoidal non-linearity as in the vertical pathway.

B Data

We used three different sets of data. Published recordings in response to the chirp stimulus (for details, see [5]) were used for model fitting. To test generalization performance, we used published recordings in response to sine flicker (for details, see [33]) as well as newly recorded responses to natural movies (see Section B.2).

B.1 Chirp

The model was trained on the cluster mean traces of the 14 BC types recorded and clustered in [5] in response to local/full-field chirp stimulus (Fig. 1C). The chirp stimulus was slightly intensity and time corrected (as in [22]) to account for slight deviations in frame rate of the projector (not exactly at 60 Hz) and an offset between digital synchronization signal ("trigger") and stimulus presentation ($\sim$34 ms), as well as for the gamma distortion of the projector.

B.2 Natural Movies

The natural movie consisted of 108 5-second sequences (64x64 pixels, $7\mu m$ pixel size) extracted from several Hollywood movies displayed at 30 Hz. Next to these "training" sequences, which were displayed in a randomized order to avoid adaptation artefacts, 5 5-second "test" sequences were displayed in a fixed order at 3 time points (beginning, middle and end). This allowed quantifying response consistency during the time of stimulus presentation. We recorded BC responses to these movies in n=1 Pvalb$^{\text{Cre}}$ mouse (Jackson laboratory, JAX 008069) using two-photon glutamate imaging in vertical optical slices (64x56 pixels @11.16 Hz) of the IPL, as described previously [34, 5]. All animal procedures were approved by the governmental review board (Regierungspräsidium Tübingen, Baden-Württemberg, Konrad-Adenauer-Str. 20, 72072 Tübingen, Germany) and performed according to the laws governing animal experimentation issued by the German Government. Regions-of-interest (ROIs) were determined using local image correlation and glutamate traces of single ROIs corresponded to the output of single BC axon terminals (for details, see [5]).

To transform the videos into 1D temporal input sequences, we fitted a difference-of-Gaussians (DoG) filter of the same spatial size as the movies:

$$\Gamma_{\sigma,K\sigma}(x,y) = I * \left(\frac{1}{2\pi\sigma^2} e^{-(x^2+y^2)/(2\sigma^2)} - \frac{1}{2\pi K^2\sigma^2} e^{-(x^2+y^2)/(2K^2\sigma^2)} \right)$$

by maximizing the correlation between the input and the recorded traces.

B.3   Sine Flicker

The sine flicker stimulus consisted of three different conditions: in the first condition the retina was stimulated with a small spot (with a diameter of $100\mu m$) with varying frequencies and intensities, in the second condition with a large spot (with a diameter of $800\mu m$) with varying frequencies and intensities and in the last condition the spot size changed additionally randomly between 10 different diameters (from 100 to $800\mu m$). The intensity varied between 10% and 100% contrast and the frequency between and 1Hz and 8Hz, all parameters were constant over trials one second. See [33] for more details.

For the stimulus of varying size we collapse the spatial dimension with a normalized one dimensional DoG filter Γ which was fitted to maximize the correlation between the stimulus and collapsed responses. The un-normalized filter had the form

$$\Gamma_{\sigma_1,\sigma_2,w}(x) = e^{-x^2/\sigma_1} - w \cdot e^{-x^2/\sigma_2} \ .$$

C   Random Search and Training Details

All models were trained using the Adam optimizer [28] and an adaptive learning rate schedule for which we performed a random search over hyperparameters. The schedule is as follows: 1) draw an initial learning rate from Log-Uniform $(0.01, 1)$; 2) Train until the loss has not increased for N steps; 3) lower the training rate by 0.5; 4) iterate over 2) and 3) for M epochs. Where (N, M) are hyperparameters that are randomly selected from $(5, 100)$ and $(3, 10)$ respectively. At $1,000$ steps the optimization was stopped regardless of convergence (most top performing models converged at around $200 - 500$ steps).

For the BCN model, we added two regularization parameters to ensure biologically plausible solutions. The first was a loss on the variance of the biphasic kernel speeds. Without this, we observed speed difference of up to 3x which is not biologically plausible (the biological range being $(1 - 1.5)$ [34]). Secondly, we also minimized the variance of the mean and variance of the release output (after the ribbon block) for each BC type. Without this loss, we had observed that the different types learned drastically different scalings (due to the scaling invariance introduced by the final normalization). This made the learned weights difficult to compare and sometimes shifted the operating range for local and global responses in an artificial way. Each of these regularizers was weighted with a hyperparameter that was included in the random search.

D   Training Results

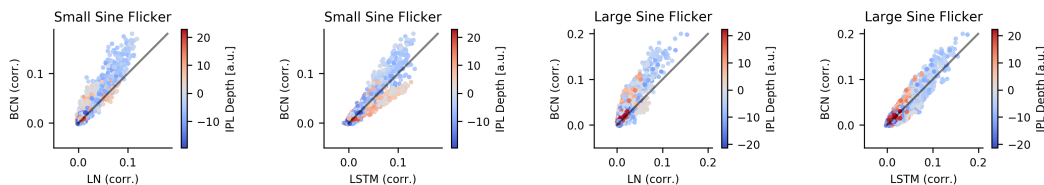#### D.1   Results for local and global flicker stimulus

Figure 7: **Generalization performance for local and global sine flicker stimulus.** Left, same as Fig. 3 A for small sine flicker stimulus. Right, same as Fig. 3 C for large sine flicker stimulus.

13

D.2   Full Training Performance

Model, Data	1	2	3a	3b	4
LN, Local	0.67	0.67	0.72	0.69	0.70
LSTM, Local	0.99	0.99	1.00	0.99	0.99
BCN, Local	0.97	0.96	0.95	0.95	0.92
LN, Global	0.53	0.71	0.69	0.45	0.58
LSTM, Global	0.99	0.99	0.99	0.99	0.98
BCN, Global	0.98	0.97	0.96	0.96	0.90

Off BC applies to the first block.

Model, Data	5t	5o	5i	X	6	7	8	9	R
LN, Local	0.67	0.67	0.72	0.69	0.70	0.86	0.83	0.84	0.85
LSTM, Local	0.99	0.99	1.00	0.99	0.99	1.00	1.00	1.00	1.00
BCN, Local	0.97	0.96	0.95	0.95	0.92	0.97	0.97	0.96	0.93
LN, Global	0.53	0.71	0.69	0.45	0.58	0.39	0.78	0.76	0.78
LSTM, Global	0.99	0.99	0.99	0.99	0.98	0.99	0.99	0.99	0.99
BCN, Global	0.98	0.97	0.96	0.96	0.90	0.95	0.98	0.97	0.95

On BC applies to the second block.

D.3   Selection of the Best Models

For later analysis we took all models within a 2% performance range of the highest correlation and under these the 20 models we took the ones with the largest weighted sum of penalty weights (β and weights for the kernel speed and variance of the release and mean output (described in C)). For the best model we took the highest penalized model within a 1% performance range.

E   Details for *in silico* Pharmacological Manipulations
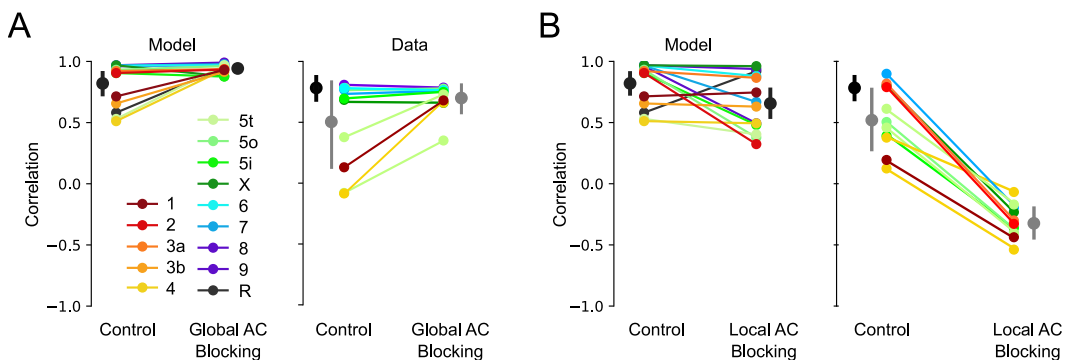
Figure 8: **Correlation between local and global traces in response to the chirp stimulus. A.** Blocking global feedback. Colors coding different BC types. For data: black dot is the mean correlation of the cluster mean traces, grey is the mean correlation of the single trials. (errorbars indicating bootstrapped 95% confidence intervals, Model: p = 0.025, paired t-test). **B.** Blocking the local feedback (Model: p = 0.036, paired t-test) All data plots are adapted from [5].

We performed three different pharmacological experiments *in silico*: (1) blocking global feedback from wide-field ACs (*in vitro* using a combination of the GABA receptor blockers TPMPA and gabazine), (2) blocking local feedback from small-field ACs (*in vitro* using the glycine receptor antagonist strychnine), and (3) selective blocking of the On BC pathway (*in vitro* using L-AP4, an agonist of the mGluR6 receptors expressed by On BCs).

Blocking of global feedback   We modified the parameters of the best model by setting $W^{\mathrm{AC_{global}BC}}$ to zero. Therefore, we blocked the global AC feedback, but the global and local models still differed by the offset parameters of the non-linearities of the vertical pathway.

14

Blocking of local feedback We modified the parameters of the best model by setting $W^{AC_{local}BC}$ and $W^{AC_{local}AC_{global}}$ to zero. Therefore we blocked the direct local feedback as well as the gating function of the local ACs for the global ACs.

Blocking of the On pathway We modified the parameters of the best model by setting the entries corresponding to the On cells of $W^{BC\ AC_{global}}$ and $W^{BC\ AC_{local}}$ to zero. Therefore we blocked the On input to both local and global ACs, and looked then only at the responses of the Off BCs.

Tonic Release Index To calculate the Tonic Release Index (TRI), we followed the definition in [5]: We took the model responses to the chirp stimulus and subtracted first the baseline for each cell (response to the stimulus step of low light intensity) to get the baseline corrected response r. We than calculated

$$\text{TRI} = \frac{\sum_t |r_-(t)|}{\sum_t |r_+(t)| + \sum_t |r_-(t)|} \ ,$$

where $r_- = r \cdot \mathbb{1}_{r<0}$ and $r_+ = r \cdot \mathbb{1}_{r>0}$.
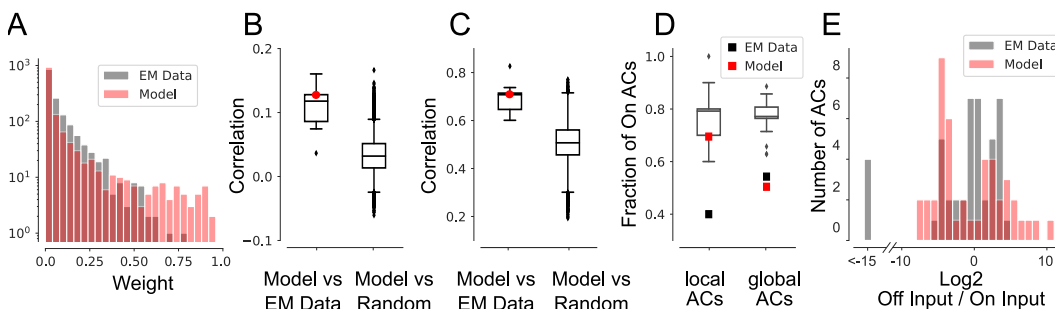
F Connectivity analysis

Figure 9: **Connectivity analysis. A.** Connectivity weight distribution after normalization for EM data and the best model. **B.** Correlation of the weight matrices between the 20 best models and the EM data/1,000 randomly sampled (and sorted) weight matrices. Red dot indicating best model. **C.** Correlation of the On/Off collapsed weight matrices (as in B) between the 20 best models and the EM data/1,000 random samples. Red dot indicating best model. **D.** Fraction of local and global ON-ACs for the EM data (black) and the mean of the 20 best models (red) and randomly sampled matrices (grey boxplot). The models did not show high variations and we omit to show the spread of the data. **E.** Histogram over Off/On input ratios for all ACs of the data and the best model.

F.1 Preprocessing of the EM data

To compare the learned model weights with the contact areas of the EM in [14], we processed the data in the following way. Firstly, we extracted contacts involving ACs and BCs (excluding ones with a contact area above 5 μm^2 as they likely do not correspond to synapses). We summarized these contacts according to cell type, resulting in a connectivity matrix of BC and AC types. We found that three types of cells (On and Off starburst amacrine cells, rod bipolar cells) dominated the matrix. Thus, we normalized the corresponding entries in the matrix such that their mean would match the mean of the remainder of the matrix (non-zero elements). As the dominant functionalities of these cell types, motion detection and signal transmission during low light levels, are not exploited by the stimulus used in our experiments, we believe this normalization step makes the comparison to the model weights more reasonable. The ACs in the "Helmstaedter dataset" are not classified as local or global ACs. Therefore, we choose 9 small-field and 1 medium-field AC (characterized in [35]), which were also identified in the Helmstaedter dataset to be local ACs. Furthermore, we verified that they used glycine as their neurotransmitter, if possible in mouse [36, 37], and otherwise in another mammalian species [38, 39]. For 8 out of the 10 cells, we were able to confirm glycine as their neurotransmitter in this way. By this procedure, we think that we separated the identified ACs in [14] into local and global ACs as good as possible with the currently limited knowledge about AC types.

15

F.2 Preprocessing of the Model Weights

Before normalizing and ordering the connectivity matrices of the model as described in the main text, we additionally adjusted the input weights to the ACs with the magnitude of the BC output. More precisely we scaled the weights of $W^{BCAC_{\text{local}}}$ and $W^{BCAC_{\text{global}}}$ which are corresponding to BC i with the standard deviation of the output of BC i. The AC to BC connections were not scaled, since the output of the ACs are all on a same scale due to the used sigmoidal non-linearity.

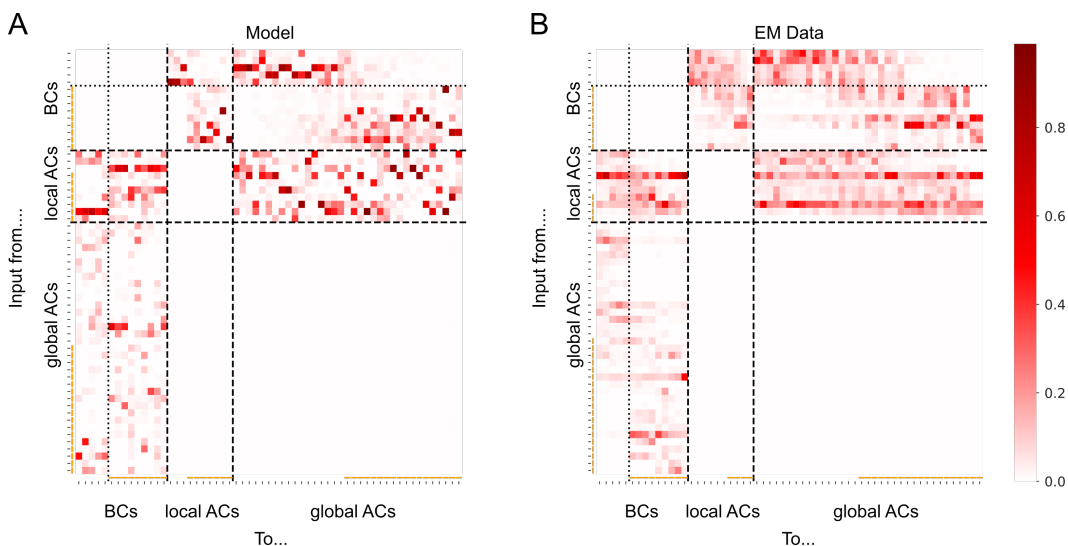## F.3 Complete Connectivity Matrices

Figure 10: **Complete connectivity matrices. A.** Weights for the best model. Orange bars indicating classification as On cell. **B.** Preprocessed connectivity matrix for the EM data. Orange bars indicating classification as On cell.